Investigation of photoelectron recapture in Ar using two-dimensional photoelectron spectroscopy

Ximao Feng,[1,*] Antony A. Wills,[1] Emma Sokell,[2] Thomas W. Gorczyca,[1] Marco Wiedenhoeft,[1] and Nora Berrah[1]

[1]*Department of Physics, Western Michigan University, Kalamazoo, Michigan 49008, USA*
[2]*Department of Experimental Physics, University College Dublin, Republic of Ireland*

"Complete" two-dimensional photoelectron spectra of Ar in the vicinity of the $2p$ ionization thresholds have been measured allowing several features in the spectra to be explained. Nine reemission series are observed and their initial and final states are determined based on the kinetic energies of these electrons. The photoelectron recapture yield above the L_2 threshold has been studied by measuring directly the reemitted electrons as a function of the photon energy. Our experimental results are found to be in reasonable agreement with our semiclassical calculations which in turn are in good agreement with the quantum-mechanical calculation of Tulkki *et al.* [Phys. Rev. A **41**, 181 (1990)].

I. INTRODUCTION

Inner-shell photoionization of atoms is very quickly followed by Auger decay of the residual core hole. If the photoionization happens close to the ionization threshold the continuum electrons may interact while still within the field of the residual ion. This is most commonly observable as an energy exchange between the slow photoelectron, which loses energy, and the fast Auger electron, which gains it. In photoelectron spectra, this energy exchange is seen as a line shift accompanied by additional lineshape broadening. This process is called postcollision interaction (PCI) [1–43].

There is a region very close to the inner-shell ionization threshold where PCI has a particularly dramatic effect on the dynamics of the ionization process. This is where the photoelectron loses more energy than its initial kinetic energy and so becomes recaptured to produce a singly charged ion state. Inner-shell $2p$ photoelectron recapture in argon has long been an important prototype system for studying photoelectron recapture probability [7,15,24–26,39]. If the photoelectron is recaptured it may still finally find itself in the continuum provided the Ar^{+*} state to which it is recaptured lies above the threshold for double ionization. If not, radiative decay is the only decay mechanism. Therefore recapture can contribute to the production of both Ar^+ and Ar^{2+} ions. Samson *et al.* [24] have shown that 67% of electrons that are recaptured at the Ar L thresholds are reemitted. These transitions between Ar^{+*} and Ar^{2+} states may also occur following resonant $2p$ excitation. In this case an initial resonant Auger decay populates the Ar^{+*} levels involved.

In the current work two-dimensional photoelectron spectra (2DPES) encompassing the $2p_{1/2,3/2}^{-1}(L_{2,3})$ thresholds in argon have been measured. This study provides a complete picture of $2p$ electron photoexcitation and photoionization in this region. The 2DPES includes photoelectrons from direct photoionization ($3s^{-1}$ and $2p^{-1}$) and Auger electrons from $2p^{-1}4s$, $md(m \geq 3)$ resonant Auger decay and $Ar^{+*}(2p^{-1})$ normal Auger decay. In addition, the 2DPES includes contributions from second-step Auger electrons after photoelectron

recapture, or reemitted electrons (above each L threshold) and second-step Auger electrons following resonant Auger decay (below each L threshold). The main goal of this work is to study photoelectron recapture using these second-step Auger electrons produced after photoelectron recapture, which have been measured for several rare gases by Refs. [44–46] and references cited therein for studying Auger cascades.

Previously [15,24], recapture curves have been generated from Ar^+ ion spectra above the $2p_{1/2}^{-1}(L_2)$ threshold. This technique only provides information about the total ion intensity without further information about the recapture process itself. The comprehensive nature of the 2DPES has allowed a photoelectron recapture curve to be extracted directly from the 2DPES. By studying the kinetic energies of the electrons we have identified the initial and final states involved in $Ar^{+*} \rightarrow Ar^{2+}$ decays. When this decay occurs above the appropriate L threshold the initial Ar^{+*} states are populated through recapture and hence a measurement of these reemitted electrons can be used to determine the recapture yield. By extracting the photoelectron yield, corresponding to two of these $Ar^{+*} \rightarrow Ar^{2+}$ decays, as a function of photon energy from the 2DPES, we have generated an experimental recapture curve that can be compared with recapture probability calculations. Our experimental results are in reasonable agreement with our semiclassical calculations which are, in turn, in good agreement with the quantum-mechanical calculation of other work [39].

II. EXPERIMENTAL METHOD

The experiment used monochromatized synchrotron radiation from the undulator beamline 10.0.1 at the Advanced Light Source (ALS) at Lawrence Berkeley National Laboratory in tandem with time-of-flight electron spectroscopy [47,48]. Since the details of the experimental setup used to perform two-dimensional, angle-resolved photoelectron spectroscopic studies are given elsewhere [48,49], only a brief description will be given here. The system consists of two time-of-flight (TOF) analyzers mounted 125.3° apart in a rotatable chamber in a plane perpendicular to the direction of the photon beam propagation. Electron TOF spectra can be

*Electronic address: ximao.feng@wmich.edu

measured simultaneously at two angles relative to the polarization plane of the incident radiation, 0° and 54.7° in this work. Argon gas was introduced into the chamber from a 0.5-mm-inner-diameter gas inlet needle which was equidistant from the two analyzers and a background pressure of typically 2×10^{-5} Torr was maintained. The energy resolution of the TOF analyzers is estimated to be 1% of the kinetic energy (KE) of the electrons in the main drift tube, after they are accelerated or decelerated. In order to collect the complete photoelectron spectrum showing all the electron emission processes in this photon energy range (approximately 246–252 eV) with acceptable resolution, the spectrum was collected in two parts. The first was optimized for the range $0 < \mathrm{KE} < 30$ eV where all low-energy electron emission occurs in this photon energy range. Here, an 11 V accelerating voltage was applied to the TOF tube to shorten the flight times of the slow electrons so those with the lowest kinetic energies could be collected within the cycle time of the photon pulses from the storage ring. The second part of the spectrum $170 < \mathrm{KE} < 225$ eV is where all the high-energy electron emission except the $3p^{-1}$ photoline is observed. The $3p^{-1}$ photoline, which corresponds to kinetic energies > 225 eV within this photon energy range, is not shown so that more detail can be seen for the rest of the spectrum. Electrons in this kinetic energy region are present in the spectrum optimized for the low-kinetic-energy region, however, the resolution for them is very poor since the kinetic energies are so large. In order to collect a 2DPES in this spectral region with optimum energy resolution while still allowing the slowest electrons in this group to reach the detector, a retarding potential of 163 V was used to reduce the electron energies.

To build up the two-dimensional photoelectron spectra, single photoelectron spectra (PES) were collected at the lowest photon energy of interest for 20 s, then the photon energy was incremented by 20 meV and another pair of PES collected. This process was repeated until the photon energy range of interest was covered. Calibration spectra of Xe [50] and Ar [51] Auger electron lines were used for the time-to-energy conversion of the electron energy axis. The photon energy scale was calibrated using the Ar $2p^{-1}4s$, $md(m \geq 3)$ resonance energies of King *et al.* [52]. The photon energy resolution was set to approximately 80 meV for this experiment. The spectra have been corrected for variations in incident photon flux.

III. RESULTS

Argon two-dimensional photoelectron spectra (2DPES) in the vinicity of the $2p$ ionization thresholds are shown in Fig. 1. More published 2DPES can be found for Ne [44], for Kr [19], and for Xe [21]. This Ar map was collected at an angle of 54.7° with respect to the polarization direction of the incident photon beam. Spectra measured at this angle display no angular effects and reflect the total cross section. Electron intensity, as a function of kinetic energy and photon energy, is represented by different shades of gray (from dark to light with a lower cutoff level below which is shown as white to provide high contrast for the weaker features).

The data were collected under two experimental conditions as described in the previous section. The kinetic energy range is almost complete, missing only values below 0.85 eV due in part to the fast electrons from the $(i+1)$th photon pulse arriving at the same time as the slowest from the ith pulse and so corrupting this part of the time spectrum. No data are shown between 26 eV and 170 eV as there are no features observerable here.

There are many resonant and nonresonant electron emission processes that are observable in this experiment. Of particular interest here are those following $2p$ ionization or resonant excitation of a $2p$ electron as illustrated schematically in Fig. 2. In trying to interpret the higher-kinetic-energy 2DPES it is useful to consider the appearance of features associated with the three emission processes that result in electrons with kinetic energies larger than 170 eV.

(1) *3s and its satellite photoionization*. Photolines are characterized by energies which vary linearly with changes in photon energy. So, when 2DPES are presented on a kinetic energy axis, photolines appear as diagonals having a slope of unity. In the case of the satellite photolines, many of which are not excited strongly in direct ionization in this photon energy region, weak signal can be seen along lines parallel to the more easily seen $3s$ photoline.

(2) *Normal Auger emission*. The lines apparent in the 2DPES above each of the $2p^{-1}$ thresholds result from the Auger decay of Ar$^+$ ions with a $2p$ vacancy [pathway (2b) in Fig. 2]. Normal Auger lines are generally characterized by fixed kinetic energies and would therefore appear parallel to the photon energy axis in Fig. 1(a). The situation is complicated in this photon energy region since the Auger lines are significantly affected by PCI. Here, they are shifted to higher kinetic energy and become broadened. Furthermore, the extent of the shift and broadening changes with increasing photon energy above the ionization threshold. The conventional one-dimensional spectrum (1DPES) above the 2DPES of Fig. 1(a) corresponds to the highest photon energy of the 2DPES and shows a more familiar spectrum. It includes photolines and the normal Auger lines.

3. *Resonant Auger emission*. The decay of a neutral, resonantly excited state to a singly charged ion [pathway (1b) in Fig. 2] also gives rise to electrons with energies, determined by the difference in energy between the Ar* and Ar$^+$ states, that are independent of the incident photon energy. At the right of Fig. 1(a) is a spectrum showing the $2p^{-1}4s$, $md(m \geq 3)$ resonances (generated by summing all electrons collected in the kinetic energy range shown for each photon energy). The dominant series is the $2p^{-1}md$ series with closelying $(m+2)s$ levels contributing a few percent of that for $2p^{-1}md$ [52,53]. For a given resonance the photon energy is well defined, though broad (≈ 100 meV) due to the short lifetime of the resonant states, and each Auger transition from such a state results in a localized increase in electron yield in the 2DPES. As several Ar$^+$ states can be populated from a single resonance state, this process shows up as a line of localized enhancements parallel to the kinetic energy axis. These resonant contributions, just below each $2p$ ionization threshold, merge into the normal Auger contributions above threshold. Care must be taken that the two contributions are
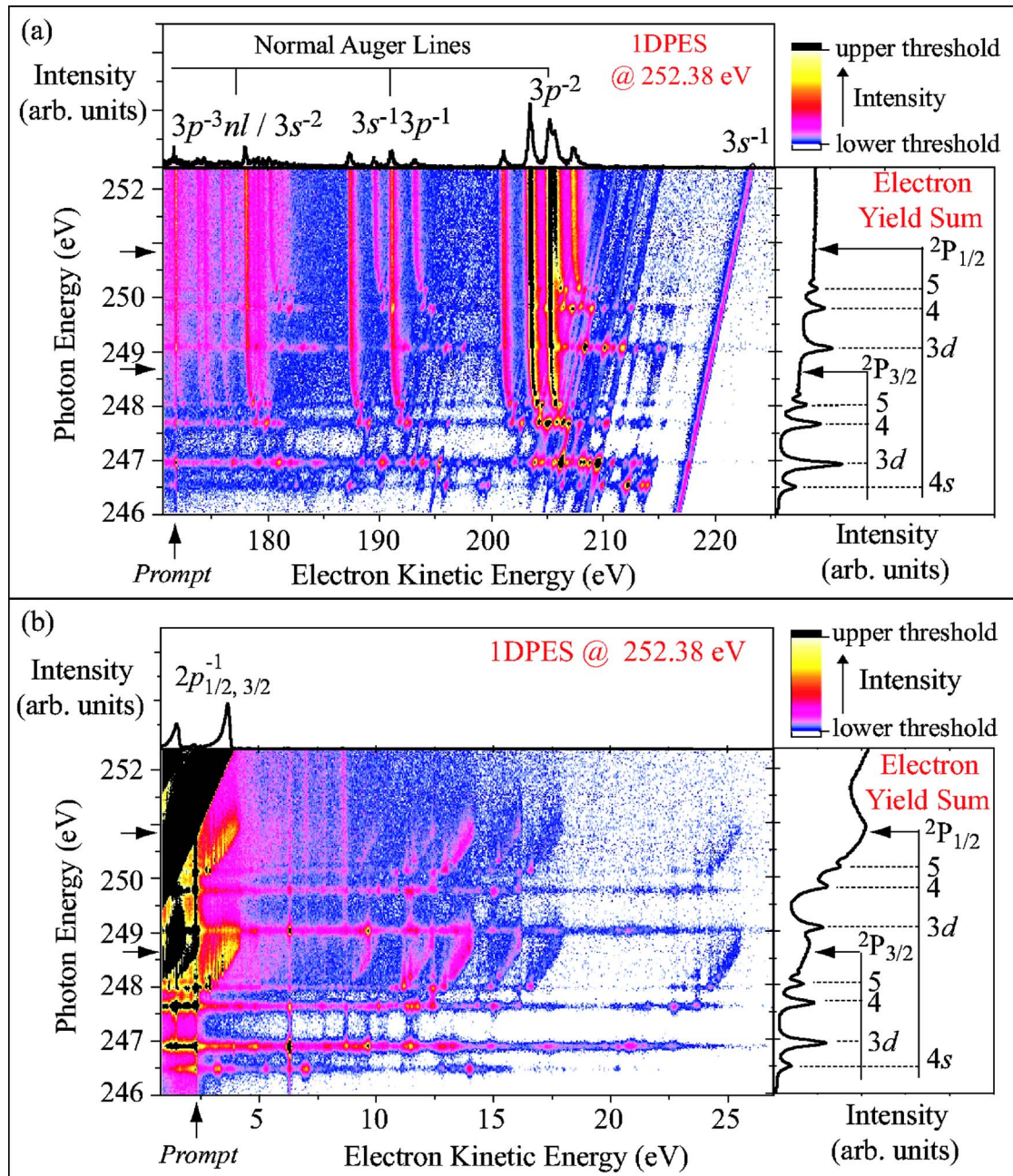
FIG. 1. (Color online) Two-dimensional photoelectron spectra (2DPES) of Ar in the vicinity of the $2p$ ionization thresholds. Different electron intensities are presented using different colors (online version) as shown by the color bars. The upper plot (a) shows the kinetic energy region >170 eV and the lower (b) the kinetic energy region <26 eV. In the right panels, spectra formed by summing all of the electron yield in the 2DPES as a function of the photon energy are shown. The conventional one-dimensional photoelectron spectra at the last photon energy values of the 2DPES are shown in the top panels. The $L_{2,3}$ thresholds are shown with horizontal arrows on both sides of the main panels. The narrow *prompt* evident in each 2DPES corresponds to photons that essentially arrive instantaneously at the detectors in the TOF analyzers. For a detailed explanation of the 2DPES see the main text.

not confused as resonant contributions can make the PCI shift of the normal Auger line appear larger than it really is.

As the kinetic energy range of Fig. 1(a) is so large, it does not show all the details of the resonant Auger decay. However, it does show the complete landscape of the resonant Auger decay of all but the lowest $2p_{3/2}^{-1}4s$ resonance, which is below the photon energy of the 2DPES of Fig. 1 [52]. It also provides an overview of the evolution of resonant into normal Auger decay. 2DPES having higher resolution for kinetic

energies above 200 eV have been presented previously [54] using a higher retarding potential than used in the current work. Also, the evolution of resonant Auger emission into the normal Auger process has been studied at ten photon energies by Aksela *et al.* [55] at even higher resolution for Kr and Xe.

The second section of the 2DPES [Fig. 1(b)] includes electrons with kinetic energies <26 eV that are produced by five significant emission processes. The photon energy of this

$$Ar(1s^2 2s^2 2p^6 3s^2 3p^6) + h\nu \xrightarrow{\text{(1a)}} Ar^*(2p^{-1}md) \xrightarrow{\text{(1b)}} Ar^{+*}((3s3p)^{-2}nd) + e_A''''$$

$$\xrightarrow[\text{(1c1)}]{} Ar^{++}((3s3p)^{-2}) + e_{auto}$$
$$\xrightarrow[\text{(1c2)}]{} Ar^+(3p^{-1}) + h\nu''$$

$$Ar(1s^2 2s^2 2p^6 3s^2 3p^6) + h\nu' \xrightarrow{\text{(2a)}} Ar^{+*}(2p^{-1}) + e_{ph}$$
$$\xrightarrow[\text{(2b)}]{} Ar^{++}((3s3p)^{-2}) + e_A'$$

$$\xrightarrow[\text{(2c1)}]{} Ar^{++}((3s3p)^{-2}) + e_A'' + e_{ph}'$$
$$\xrightarrow[\text{(2c2)}]{} Ar^{+*}((3s3p)^{-2}nd) + e_A'''$$

$$\xrightarrow[\text{(2d1)}]{} Ar^{++}((3s3p)^{-2}) + e_{re}$$
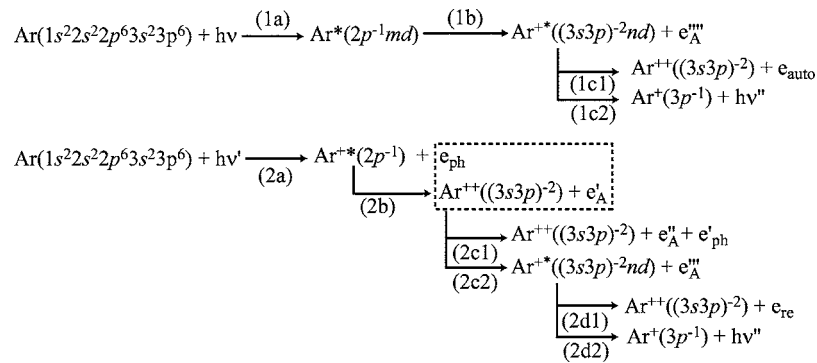$$\xrightarrow[\text{(2d2)}]{} Ar^+(3p^{-1}) + h\nu''$$

FIG. 2. Decay channels after $2p \rightarrow md$ photoexcitation and $2p^{-1}$ photoionization in Ar. The dashed rectangle indicates the initial state for the PCI process. $(3s3p)^{-2}$ is a collective notation for states with two electrons missing from the $3s$ and/or $3p$ orbital(s). e_{re} stands for a reemission electron, e_{auto} stands for an autoionization electron, e_A for an Auger electron, and e_{ph} for a photoelectron. Primes are used to distinguish electrons and photons with different energies. Possible decay routes from Ar^{2+} to more highly charged ion states are not shown.

experiment is sufficient to produce Ar^{4+} ions but since the probabilities for production become progressively smaller as the charge state increases [24] they will not be mentioned further.

(1) *2p photoionization.* The $2p$ photolines [pathway (2a) in Fig. 2] appear in the top left-hand corner of Fig. 1(b) and can be seen in the 1DPES above the 2DPES. These lines curve from diagonal paths due to PCI and the kinetic energy of the electrons decreases more rapidly than the incident photon energy as threshold is approached from above. However, this curvature is difficult to see on the scale of the figure.

(2) *Shake-off of two electrons.* In addition to the normal Auger emission seen at high kinetic energies following $2p$ ionization, two electrons may be simultaneously ejected (*shake-off*). This results in the electrons sharing the available energy between themselves and gives rise to a general increase in the real continuous electron background in the 2DPES once the ionization threshold is reached.

(3) *Resonant shake-off of two electrons.* A similar process can also occur following resonant excitation of a $2p$ electron. In this case the general increase in electron yield will appear as a band parallel to the kinetic energy axis at the photon energy of the resonance.

(4) *Second-step normal Auger emission.* Two electrons can also be produced following $2p$ ionization when the Ar^{2+} state populated by normal Auger decay of the $2p$ hole, lies energetically above the Ar^{3+} threshold. Since the decay rate for this second-step normal Auger process is slow compared to the inner-shell case, the energies of these electrons are unaffected by PCI. These lines are consequently of constant kinetic energy, parallel to the photon energy axis on the 2DPES. The kinetic energies are comparatively small, occurring in the <10 eV range.

(5) *Second-step resonant Auger emission.* There is another second-step Auger process of particular interest to the current work, this occurs following the resonant Auger decay discussed above. Like the second-step normal Auger decay this resonant process gives rise to comparatively low-kinetic-energy electrons (<26 eV) and is responsible for much of the structure in the 2DPES of Fig. 1(b).

At this point it is useful to consider the last process in detail. Figure 3(a) shows two resonant Auger decay steps to

a particular Ar^{2+} state. It is not to scale since $E(e_A''')$ >170 eV while $E(e_{auto}) < 26$ eV and only a few of the many potential decays at each step are shown for the sake of clarity. As the $2p$ ionization threshold is reached, corresponding to larger values of the principal quantum number of the Rydberg electron [pathway (1a) in Fig. 2], the energy of the first Auger electron [pathway (1b)] decreases, provided that the principal quantum number of the Rydberg electron does not change significantly during the Auger emission process. This is because, for equivalent values of the principal quantum number, the energy level spacing is larger in the ion than in the neutral atom. As the principal quantum number of the Rydberg electron in the Ar^+ ion increases the energy of the second-step Auger electron [low kinetic energy, pathway (1c1)] increases, for decays to a particular Ar^{2+} state. For Ar^+ states below the Ar^{2+} threshold only radiative decay [pathway (1c2)] is possible.

In reality the picture is more complicated as each Auger decay step populates a variety of levels although certain trends have been noted. At low levels of resonant excitation shake-up transitions dominate while as the principal quantum number increases towards the ionization limit shake-down becomes dominant [55]. Therefore, not only do the initial resonances populate a range of states (in both first- and second-step Auger decays) but many of these transitions can be observed over a range of resonances. This can be seen quite nicely from the 2DPES. The increase in energy of the electrons associated with the most favored second-step Auger transition means that the second-step process gives rise to diagonal features in the 2DPES. Each diagonal feature corresponds to members of a particular Ar^{+*} Rydberg series decaying to an Ar^{2+} state. Figure 1(b) shows two sets of prominent diagonal features, each set associated with one of the L thresholds. Nine Rydberg series can be observed on the kinetic energy scale at each threshold. Table I lists the 15 energetically allowed series. From the reported Ar Auger line energies [51], one can derive the limits of all 15 series. Comparing these with the limits obtained from the 2DPES, we can conclude that the observable series are the nine numbered series S1 to S9 in Table I. Table II shows their limits extracted from our 2DPES and those derived from Ref. [51]. The other six series, Sa–Sf, do not give rise to significant features in the 2DPES.
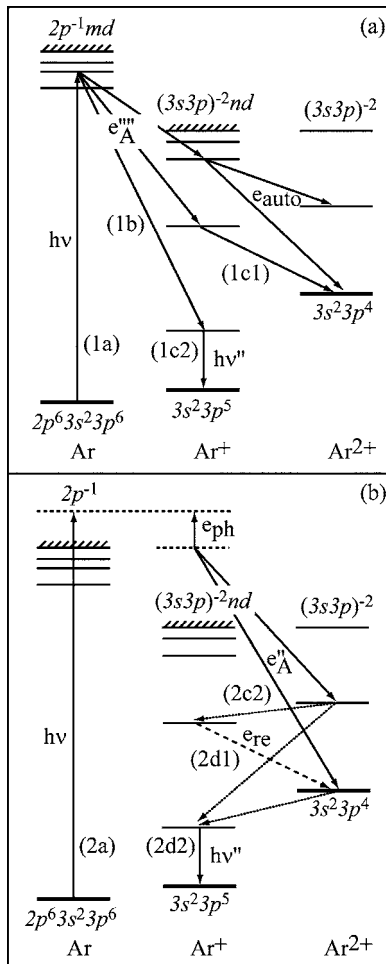
FIG. 3. Decay processes that lead to (a) second-step resonant Auger electrons in the resonant pathway and (b) reemitted electrons in the recapture pathway following $2p$ ionization. For equivalent transitions the kinetic energies of the e_{auto} and e_{re} electrons are the same. The labels of the type (1a) are those used in Fig. 2 to identify the decays.

Electron reemission. Once the $2p$ ionization threshold is reached the Ar^{+*} states, which are the initial states for the series S1–S9, are no longer accessible via Auger decay. The vacancy in the $2p$ shell is quickly filled with the emission of a high-energy normal Auger electron [pathway (2b) in Fig. 2]. It would therefore be expected that second-step resonant

TABLE I. Possible autoionization-reemission series in Ar around the $2p$ thresholds.

Final state		Initial state					
		$3s^0 3p^6$	$3s^1 3p^5$		$3s^2 3p^4$		
		$(^1S)nd$	$(^1P)nd$	$(^3P)nd$	$(^1S)nd$	$(^1D)nd$	
$3s^1 3p^5$	(^1P)	Sc					
	(^3P)	Sd	Sa				
$3s^2 3p^4$	(^1S)	Se	Sb	S4			
	(^1D)	S9	S7	S5	S2		
	(^3P)	Sf	S8	S6	S3	S1	

TABLE II. Limits of the nine autoionization-reemission series observed in the Ar 2DPES.

	Series limit	
Series name	These data	From Ref. [51]
S1	1.56	1.74[a]
S2	2.29	2.38
S3	4.07	4.12[a]
S4	10.01	9.96
S5	12.46	12.34[a]
S6	14.12	14.08[a]
S7	16.18	16.14
S8	17.84	17.88[a]
S9	25.60	25.56

[a]P_2 is used for $^3P_{2,1,0}$.

Auger decay will not be apparent in the 2DPES once $2p$ ionization occurs. However, PCI can cause the slow photoelectron to lose sufficient energy that it is recaptured [pathway (2c2) in Fig. 2 and Fig. 3(b)]. The resulting Ar^{+*} levels are the same as those populated in the two-step resonant Auger decay [Fig. 3(a)]. Therefore, any signal from the decay of Ar^{+*} states at photon energies higher than the resonant excitation region arises from reemission of recaptured electrons. The continuation of the diagonal features above the $2p$ thresholds is evident in Fig. 1(b).

The current experiment is able to probe the recapture process further since the photoelectron spectra contain information on the particular Ar^{+*} levels that are populated by the recapture process. Unfortunately the energy resolution and statistics are not sufficient to make as wide-ranging and quantitative a study of this as might be thought looking at Fig. 1(b). However it does indicate where future studies might focus. Figure 1(b) shows that the signal in the region of the spectrum where the second-step Auger decay is well separated from other features (S9) is quite weak and at a comparatively poor resolution due to the higher kinetic energy of the electrons. However, by concentrating on the region of the 2DPES containing electrons associated with emission from series S7 and S8 the recapture yield associated with these two series of Ar$^{+*} \rightarrow$ Ar^{2+} decay pathways can be investigated.

A 2DPES detailing this region is shown in Fig. 4. This spectrum was collected at an electron emission angle of 54.7° and concentrates on the kinetic energy range incorporating the series S4–S8 and extends to a higher photon energy than Fig. 1. The series limits of the five series S4–S8 are marked above the main panel in the new 2DPES. From this figure, we can see the existence of these series at both the L_2 and L_3 thresholds and their continuation across the thresholds.

Figure 5 shows more details in the region of S7 and S8. Localized increases in electron yield associated with second-step resonant Auger decay between Rydberg states with relatively small values of the principal quantum number are labeled in Fig. 5. The initial states for both S7 and S8 are the Ar$^{+*}(3s^1 3p^5)(^1P)nd$ states. Armen and Larkins [56,57] have
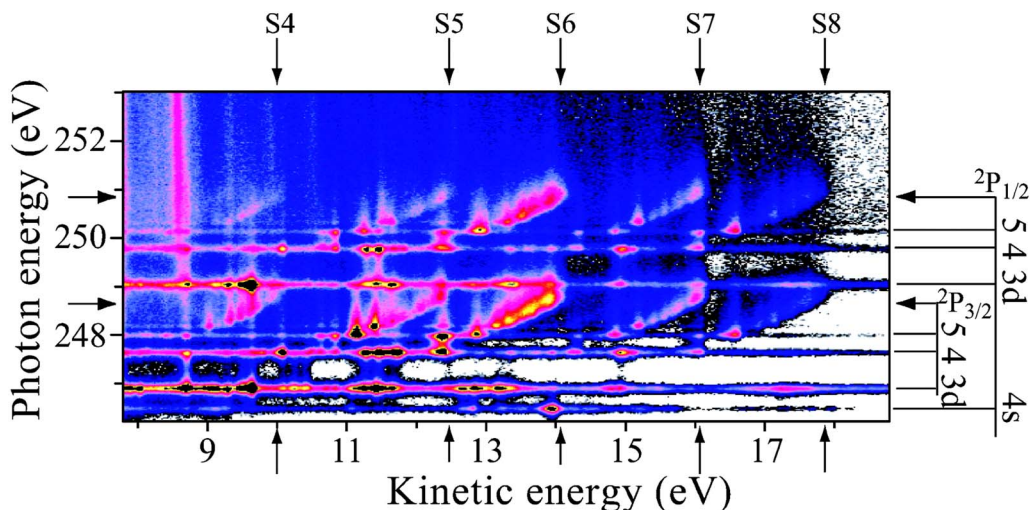
FIG. 4. (Color online) An Ar 2DPES collected at 54.7° showing in detail five of the nine electron autoionization-reemission series S4–S8. These series limits are indicated by vertical arrows in the figure. Horizontal arrows indicate the $L_{2,3}$ thresholds. The $2p^{-1}$ resonances are marked at the right of the 2DPES.

calculated the rates for radiative and nonradiative decay from these states and predict that if electron emission is energetically possible it will be the dominant decay path. In this case electron emission is possible for even the lowest members of the series [58] and hence the radiative decay pathway can be ignored. Similarly, if these $Ar^{+*}(3s^13p^5)nd$ states are populated through recapture of a photoelectron above the relevant $2p$ threshold a measurement of the reemission yield [pathway (2d1) in Fig. 2] is equivalent to a determination of the recapture yield for the states that give rise to series S7 and S8. This sort of discrimination is not possible in studies concerned with the measurement of photoion yield. The rectangle drawn around S7 and S8 in Fig. 5 shows the area into which the majority of the reemission yield from these two series falls. In order to compare the experimental data with calculations an excitation function (EXF) was obtained by projecting all of the electron yield within the rectangle onto the photon energy axis. The area of the L_2 threshold has been chosen because the region immediately above this threshold is free from resonant states.

IV. THEORETICAL CONSIDERATIONS

Several semiclassical and quantum-mechanical models have been presented to calculate photoelectron recapture probability after $2p$ ionization in Ar during the past 30 years [15,30,33–41]. Although quantum-mechanical calculations have been shown to be in better agreement with experimental results [39], semiclassical calculations are still used frequently due to their simplicity. In this section, we report on our semiclassical calculations based on previous work [15,35,41]. In the classical picture, the recapture process can be described in the following way. At time $t=0$, a $2p$ electron is photoionized at the classical minimum distance $r_{\min}$ from the nucleus and gains the excess energy $E_{exc}=h\nu-E_b$, where E_b is the binding energy of $2p$ electrons. For electric dipole transitions, the selection rule $\Delta l = \pm 1$ allows the photoelec-

tron to be either a d wave ($l_{ph}=2$) or an s wave ($l_{ph}=0$). Subsequently, an energetic Auger electron with energy E_A is ejected, passing the photoelectron at a distance $r_{\max}$ from the nucleus. In this process, the potential experienced by the photoelectron can be described by the effective potential as a function of its distance from the nucleus:

$$V_{eff}(r) = -\frac{Z}{r} + \frac{L^2}{2r^2}, \tag{1}$$

which is made up of the Coulomb potential, due to the interaction of the photoelectron and the nucleus, $-Z/r$, and the "centrifugal barrier" potential, $L^2/(2r^2)$. Equation (1) is in atomic units and these units will be used in all other equations in this work. In Eq. (1), Z is the charge of the nucleus seen by the photoelectron, which is 1 before the Auger electron passes and 2 afterwards, and $L=\sqrt{l(l+1)}$ is the orbital angular momentum of the photoelectron. After the Auger electron passes the photoelectron, the latter experiences a sudden potential change from $V_{eff}=-1/r_{\max}+L^2/2r^2$ to V'_{eff}
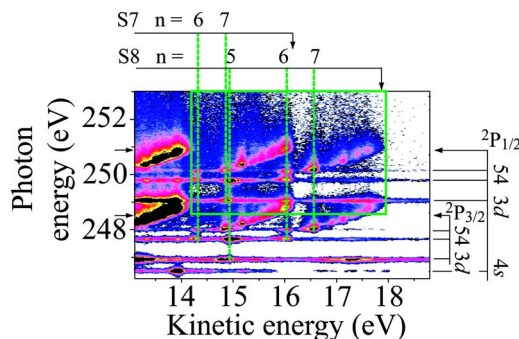

FIG. 5. (Color online) Detailed part of Fig. 4 in the region of S7 and S8 at the L_2 threshold formed by electrons in the decay of $Ar^{+*}3s^13p^5(^1P)nd \rightarrow Ar^{2+}3s^23p^4(^1D,{}^3P)+e_{auto}/e_{re}$ [see (1c1) and (2d1) in Fig. 2]. The rectangle around S7 and S8 encloses the area of interest used to obtain the EXF described in the text.

TABLE III. Summary of the eight different calculations for photoelectron recapture probability. In the first two calculations t_A was assumed to be zero. All possible values of l for the photoelectron and the Auger electron have been used in the calculation of t_{ph} and t_A.

Formula	l_{ph}	l_A	Result
$P = 1 - \exp[-\Gamma(t_{ph})]$	2		P_1
	0		P_2
$P = 1 - \exp[-\Gamma(t_{ph} - t_A)]$	2	0	P_3
		1	P_4
		2	P_5
	0	0	P_6
		1	P_7
		2	P_8

$= -2/r_{max} + L^2/2r^2$ because of the screening change. Thus, its excess energy decreases by the same amount as the potential energy difference, $1/r_{max}$. If $1/r_{max}$ is larger than E_{exc}, the new excess energy of the photoelectron, $E'_{exc} = E_{exc} - 1/r_{max}$, becomes negative, and the photoelectron is recaptured by the ion. For a hole state of width Γ, the probability that the Auger electron is emitted at a time not longer than τ is given by [39]:

$$P(\tau) = 1 - \exp(-\Gamma\tau). \tag{2}$$

In the classical model, recapture will occur if

$$\tau = t_{ph} - t_A, \tag{3}$$

where t_{ph} and t_A are, respectively, the times it takes the slow photoelectron and the fast Auger electron to reach the distance r_{max} from the nucleus.

Thus, the photoelectron recapture probability can be expressed as

$$P = 1 - \exp[-\Gamma(t_{ph} - t_A)]. \tag{4}$$

In order to calculate t_{ph} and t_A, we use the fact that energy of both the photoelectron and Auger electron satisfy the equation below:

$$\frac{1}{2}v^2 = E - \left[-\frac{Z}{r} + \frac{L^2}{2r^2} \right]. \tag{5}$$

In Eq. (5), the left side is the kinetic energy while on the right side, the first term is the total energy and the second term is the effective potential of Eq. (1). For the photoelectron, the total energy is E_{exc} and $Z=1$. For the Auger electron, $E=E_A$ and $Z=2$. Combining Eq. (5) and $v = dr/dt$, we obtain

$$t = \sqrt{\frac{1}{2}} \left[\frac{\sqrt{Er^2 + Zr - L^2/2}}{E} - \frac{Z}{2E^{3/2}} \ln[2\sqrt{E(Er^2 + Zr - L^2/2)} \right.$$
$$\left. + 2Er + Z] \right]_{r_{min}}^{r_{max}}. \tag{6}$$

From the above discussion, the photoelectron will be recaptured provided E_{exc} is not larger than $1/r_{max}$. Therefore, the
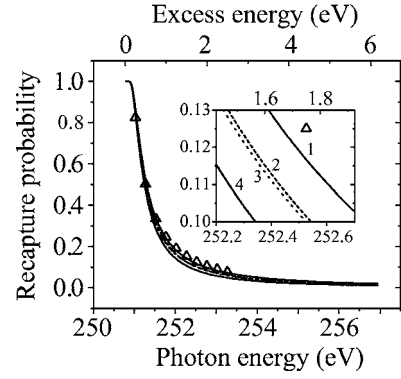

FIG. 6. Our semiclassical calculations (solid lines) of the photoelectron recapture probability as a function of both the photon energy and the excess energy compared with the quantum-mechanical calculation data points from Ref. [39] (empty triangles). The inset shows the curve sections in the photon energy range of 252.2 eV ~ 252.7 eV. In this figure the numbers of the curves correspond to the calculation results in Table III according to the following scheme: 1, P_1; 2, P_2; 3, P_3, P_4, and P_5; 4, P_6, P_7, and P_8.

limiting condition for the photoelectron to be recaptured is

$$r_{max} = 1/E_{exc}. \tag{7}$$

By solving Eq. (5) with $v=0$ and $r=r_{min}$, we obtain r_{min}:

$$r_{min} = \frac{\sqrt{Z^2 + 2EL^2} - Z}{2E}. \tag{8}$$

Substituting Eqs. (7) and (8) into Eq. (6), we obtain the following general formula to calculate both t_A and t_{ph}:

$$t = \frac{\sqrt{E/E_{exc}^2 + Z/E_{exc} - L^2/2}}{\sqrt{2}E}$$
$$- \frac{Z}{(2E)^{3/2}} \ln\left(\frac{2\sqrt{E(E/E_{exc}^2 + Z/E_{exc} - L^2/2)} + 2E/E_{exc} + Z}{\sqrt{Z^2 + 2EL^2}} \right). \tag{9}$$

Depending on whether we assume that t_A in Eq. (4) is zero (corresponding to the Auger electron instantaneously reaching r_{max}) or not and what values of L are used in Eq. (9) to calculate t_A and t_{ph}, we obtained eight different recapture probabilities. The different values of the parameters used for calculating these results are shown in Table III and all eight results are plotted in Fig. 6. One of the results, P_1, is shown here as an example:

$$P_1 = 1 - \exp(-\Gamma t_{ph}) = 1 - \left(\frac{\sqrt{1 + 12Eexc}}{2\sqrt{2 - 3E_{exc}} + 3} \right)^{-\Gamma/(2E_{exc})^{3/2}}$$
$$\times \exp\left(-\frac{\Gamma\sqrt{2 - 3E_{exc}}}{\sqrt{2}E_{exc}^{3/2}} \right) \tag{10}$$

Figure 6 shows all our calculations of the Ar $2p$ photoelectron recapture probability as a function of the photon energy. From the figure, we can see that all the curves are very similar. Calculations P_3, P_4, and P_5 are not distinguishable even on the scale of the inset. The same is true for
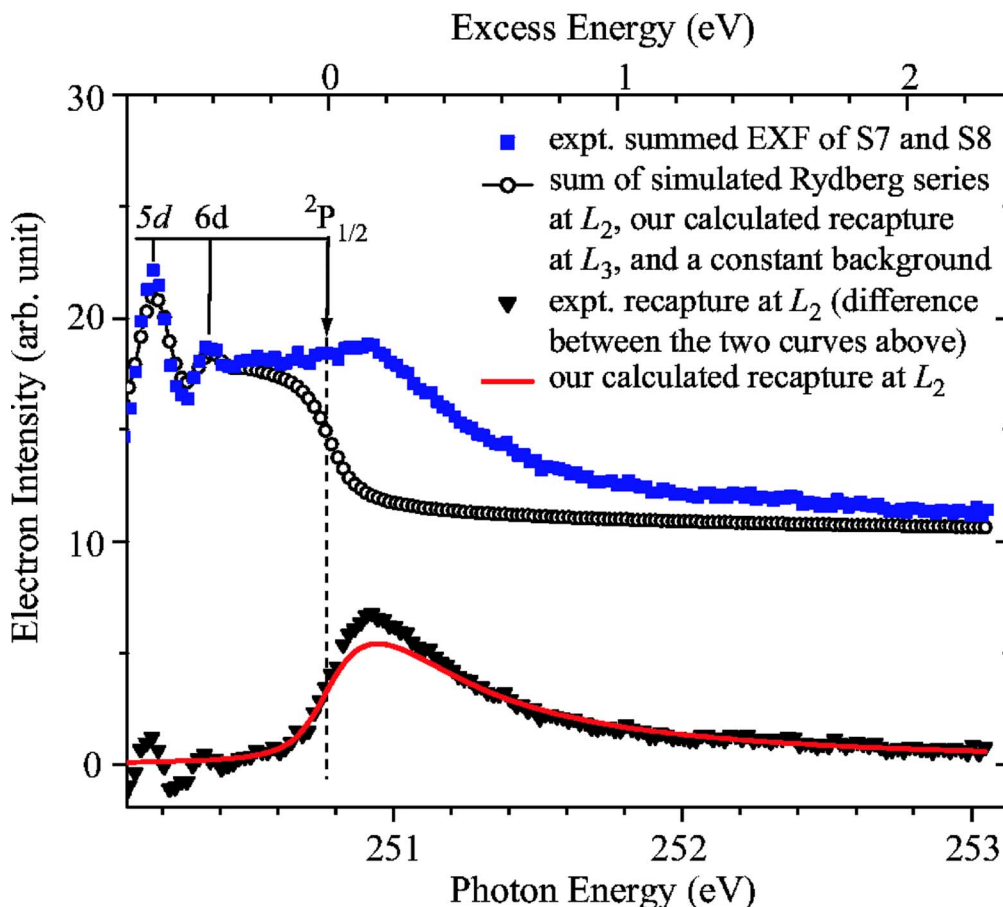
FIG. 7. (Color online) Experimental photoelectron recapture curve at L_2 threshold (full inverted triangles) at 54.7° extracted from the summed EXF of S7 and S8 (full squares) compared with our calculated recapture yield Eq. (10) after convolution (line). The experimental recapture yield at the L_2 threshold was obtained by subtracting the sum of the simulated Rydberg series converging on the L_2 threshold, the calculated L_3 recapture probability and a constant background (empty circles) from the extracted EXF. The vertical dashed line shows the L_2 threshold.

calculations P_6, P_7, and P_8. This shows that the angular momentum of the Auger electron does not have much effect on the recapture probability. The main difference between the calculations occurs in the middle section (251–254 eV). The biggest difference is about 5% between calculation P_1 and calculation P_6 at a photon energy of 252.3 eV. For comparison, the quantum-mechanical calculation of Ref. [39] has also been plotted in the figure. The agreement between the two calculations is good, although the quantum-mechanical calculations do not extend to energies below 0.25 eV.

To compare meaningfully with experiment, the intrinsic width of the $2p$ hole state and the photon energy distribution profile need to be considered. In this case, the intrinsic width has been modelled using a Lorentzian of width 126 meV [59] and a Gaussian function of full width at half maximum of 80 meV has been used for the photon energy profile. Tulkki *et al.* [39] simply convoluted their calculations with the appropriate photon energy profile when comparing with the experimental data of Eberhardt *et al.* [15]. However, as the recapture probability is a function of the energy of the photoelectron this simple convolution is not strictly correct. Photoelectrons with a range of energies will be produced at a given photon energy and consequently there will be a corresponding range of recapture probabilities.

V. DISCUSSION

An excitation function (EXF) of the sum of S7 and S8 extracted from Fig. 5 is shown in Fig. 7. These second-step electrons can either be due to reemission following recapture [pathway (2d1) in Fig. 2] or second-step resonant Auger emission [pathway (1c1)]. Consequently the EXF contains reemission contributions from each of the L_3 and L_2 continua, resonant Auger contributions produced via population of neutral Rydberg states converging on the L_2 threshold and a constant background. All of these contributions must be accounted for when comparisons are made between experiment and calculations.

To account for the resonant contribution from pathway (1c1) we have simulated the appropriate Rydberg series. We have assumed that the second-step electron yield has the same profile as that of the initial Ar $2p \rightarrow md$ resonances, the scale being the only difference between them. Thus, we can simulate a Rydberg series for the $2p \rightarrow md$ resonances, and normalize this simulated curve to the experimental EXF of S7 and S8. The $2p \rightarrow md$ resonance positions can be determined using the following equation:

$$E(m) = \mathcal{P}_{\text{ion}} - \frac{Z^2}{2(m^*)^2}, \qquad (11)$$

where $\mathcal{P}_{\text{ion}}$ represents the ionization potential, Z the charge seen by the electron at the Rydberg orbital (in this case, $Z = 1$), and m^* the effective quantum number with $m^* = m - \alpha(l) - \beta(l)/m^2$. From the effective quantum numbers given in Ref. [52], we derived the values for the two quantum defect parameters α and β and used them to calculate values for m^* for all the resonances. The Lorentzian formula

$$y = y_0 + \frac{2A}{\pi} \frac{w}{4(x - x_c)^2 + w^2} \qquad (12)$$

was used to calculate the yield for each resonance which is applied with a factor of $(m^*)^{-3}$. In these calculations, we used 126 meV for w. This value for the intrinsic linewidth is the same as that used in Ref. [39] for the width of the $2p^{-1}$ inner-shell hole state, which is the limiting case for the resonances we are modeling. Finally, we summed all the resonances ($m = 3 \rightarrow 500$) (the upper limit is large enough to approximate infinity) to obtain the simulated Rydberg series, which was then convoluted with the 80 meV photon energy profile.

The extracted EXF shown also includes contributions from recapture at the L_3 threshold, which should be the same shape (relative to the ionization threshold) but twice as intense as the L_2 recapture contribution due to the statistical weights associated with the two spin-orbit states. In argon the L_3 threshold is 2.03 eV lower ([15] and references therein). A single factor has been used to scale the recapture calculations to the experimental data and the L_3 contribution weighted by an additional factor of 2. This L_3 recapture contribution, the simulated Rydberg series and an appropriate constant background have been removed from the experimental data shown to leave the experimental recapture yield at the L_2 threshold. A simulated curve containing these three contributions and the experimental recapture yield at the L_2 threshold are both shown in Fig. 7. The background contribution was determined by comparing the simulated curve to the extracted EXF at the $2p \rightarrow 6d$ resonance where the recapture contribution at the L_2 threshold can be ignored. From the figure, one can see that there is some discrepancy between the simulated curve and the summed experimental electron yield for the low $2p \rightarrow md$ resonances. This is due mainly to the simplicity of the approach used for the simulation of the Rydberg resonance series which is only valid for larger m. Since the threshold region is the main interest here, these limitations should not significantly affect comparison of the calculated and experimental recapture yields. The calculated recapture yield curve of P_1, after convolution with the $2p$ core-hole width and the finite photon energy width, is shown in Fig. 7. Although the general agreement is good, our calculation has some apparent discrepancy with the experimental data at excess energies below approximately 0.5 eV. The calculations appear to underestimate the recapture yield.

From among all our calculations (Fig. 6) P_1 is in the best agreement with our experimental curve. Therefore we can conclude that the vast majority of the photoelectrons are ejected as d-waves and that it is not necessary to take into account the time for the fast Auger electron to catch up with the slow photoelectron in the classical picture. The good general agreement between the calculations, which do not specify the states to which the recapture occurs, and the experimental data, which originates from recapture into $Ar^+3s^13p^5(^1P)nd$ states, suggests that the probability for recapture is independent of the Ar^{+*} states involved.

VI. CONCLUSION

We have presented 2DPES of Ar in the region of its $L_{2,3}$ ionization thresholds. The 2DPES technique reveals a comprehensive picture of atomic photoexcitation and photoionization in this richly structured spectral region. Extracting data from the 2DPES has allowed us to obtain an experimental photoelectron recapture curve by directly measuring the reemitted electrons. The experimental curve is in good general agreement with our classical calculation in which the time for the Auger electron to overtake the d-wave photoelectron is ignored. Our calculations are also in very good agreement with Tulkki $et\ al.$'s tabular data points calculated with a quantum-mechanical method [39]. Measuring the reemitted electrons directly provides a clearer picture of the process than that obtained by measuring ions. It also has the potential to provide detailed information about the states (Ar^{+*} and Ar^{2+}) involved in secondary Auger decay.

---

[1] R. B. Barker and H. W. Berry, Phys. Rev. **151**, 14 (1966).

[2] P. J. Hicks, S. Cvejanović, J. Comer, F. H. Read, and J. M. Sharp, Vacuum **24**, 573 (1974).

[3] H. G. M. Heideman, G. Nienhuis, and T. van Ittersum, J. Phys. B **7**, L493 (1974).

[4] H. G. M. Heideman, T. van Ittersum, G. Nienhuis, and V. M. Hol, J. Phys. B **8**, L26 (1975).

[5] A. J. Smith, P. J. Hicks, F. H. Read, S. Cvejanović, G. C. M. King, J. Comer, and J. M. Sharp, J. Phys. B **7**, L496 (1974).

[6] G. Nienhuis and H. G. M. Heideman, J. Phys. B **8**, 2225 (1975).

[7] M. J. van der Wiel, G. R. Wight, and R. R. Tol, J. Phys. B **9**,

L5 (1976).

[8] V. Schmidt, N. Sandner, and W. Mehlhorn, J. Phys. B **38**, 63 (1977).

[9] H. Hanashiro, Y. Suzuki, T. Susaki, A. Mikuni, T. Takayanagi, K. Wakiya, H. Suzuki, A. Danjo, T. Hino, and S. Ohtani, J. Phys. B **12**, L775 (1979).

[10] V. Schmidt, S. Krummacher, F. Wuilleumier, and P. Dhez, Phys. Rev. A **24**, 1803 (1981).

[11] S. Southworth, U. Becker, C. M. Truesdale, P. H. Kobrin, D. W. Lindle, S. Owaki, and D. A. Shirley, Phys. Rev. A **28**, 261 (1983).

[12] T. Hayaishi, Y. Morioka, Y. Kageyama, M. Watanabe, I. H. Suzuki, A. Mikuni, G. Isoyama, S. Asaoka, and M. Nakamura, J. Phys. B **17**, 3511 (1984).

[13] M. Borst and V. Schmidt, Phys. Rev. A **33**, 4456 (1986).

[14] P. A. Heimann *et al.*, J. Phys. B **20**, 5005 (1987).

[15] W. Eberhardt, S. Bernstorff, H. W. Jochims, S. B. Whitfield, and B. Crasemann, Phys. Rev. A **38**, 3808 (1988).

[16] T. Hayaishi, E. Murakami, A. Yagishita, F. Koike, Y. Morioka, and J. E. Hansen, J. Phys. B **21**, 3203 (1988).

[17] L. Avaldi, R. I. Hall, G. Dawber, P. M. Rutter, and G. C. King, J. Phys. B **24**, 427 (1991).

[18] K. Ueda, E. Shigemasa, Y. Sato, A. Yagishita, M. Ukai, H. Maezawa, T. Hayaishi, and T. Sasaki, J. Phys. B **24**, 605 (1991).

[19] D. Čubrić, A. A. Wills, J. Comer, and M. A. MacDonald, J. Phys. B **25**, 5069 (1992).

[20] J. A. de Gouw, J. van Eck, J. van der Weg, and H. G. M. Heideman, J. Phys. B **25**, 2007 (1992).

[21] D. Čubrić, A. A. Wills, E. Sokell, J. Comer, and M. A. Mac-Donald, J. Phys. B **26**, 4425 (1993).

[22] L. Avaldi, G. Dawber, R. Camilloni, G. C. King, M. Roper, M. R. F. Siggel, G. Stefani, and M. Zitnik, J. Phys. B **27**, 3953 (1994).

[23] J. A. de Gouw, J. van Eck, J. van der Weg, and H. G. M. Heideman, J. Phys. B **28**, 1761 (1995).

[24] J. A. R. Samson, W. C. Stolte, Z. X. He, J. N. Cutler, and D. Hansen, Phys. Rev. A **54**, 2099 (1996).

[25] J. A. R. Samson, Y. Lu, and W. C. Stolte, Phys. Rev. A **56**, R2530 (1997).

[26] Y. Lu, W. C. Stolte, and J. A. R. Samson, Phys. Rev. A **58**, 2828 (1998).

[27] W. Kuhn, B. Feuerstein, and W. Mehlhorn, J. Phys. B **34**, 2835 (2001).

[28] T. Hayaishi, T. Matsui, H. Yoshii, A. Higurashi, E. Murakami, A. Yagishita, T. Aoto, T. Onuma, and Y. Morioka, J. Phys. B **35**, 141 (2002).

[29] D. L. Hansen, W. C. Stolte, O. Hemmers, R. Guillemin, and D. W. Lindle, J. Phys. B **35**, L381 (2002).

[30] G. C. King, F. H. Read, and R. C. Bradford, J. Phys. B **8**, 2210 (1975).

[31] F. H. Read, J. Phys. B **10**, L207 (1977).

[32] R. Morgenstern, A. Niehaus, and U. Thielmann, J. Phys. B **10**, 1039 (1977).

[33] A. Niehaus, J. Phys. B **10**, 1845 (1977).

[34] M. Y. Amusia, M. Y. Kuchiev, S. A. Sheinerman, and S. I. Scheftel, J. Phys. B **10**, L535 (1977).

[35] A. Russek and W. Mehlhorn, J. Phys. B **19**, 911 (1986).

[36] G. B. Armen, S. L. Sorensen, S. B. Whitfield, G. E. Ice, J. C. Levin, G. S. Brown, and B. Crasemann, Phys. Rev. A **35**, 3966 (1987).

[37] G. B. Armen, J. Tulkki, T. Åberg, and B. Crasemann, Phys. Rev. A **36**, 5606 (1987).

[38] G. B. Armen, Phys. Rev. A **37**, 995 (1988).

[39] J. Tulkki, T. Åberg, S. B. Whitfield, and B. Crasemann, Phys. Rev. A **41**, 181 (1990).

[40] G. B. Armen, J. C. Levin, and I. A. Sellin, Phys. Rev. A **53**, 772 (1996).

[41] G. B. Armen and J. C. Levin, Phys. Rev. A **56**, 3734 (1997).

[42] G. B. Armen, S. H. Southworth, J. C. Levin, U. Arp, T. LeBrun, and M. A. MacDonald, Phys. Rev. A **56**, R1079 (1997).

[43] S. A. Sheinerman, J. Phys. B **36**, 4435 (2003).

[44] R. Hentges, N. Müller, J. Viefhaus, U. Heinzmann, and U. Becker, J. Phys. B **37**, L267 (2004), and references therein.

[45] A. D. Fanis, G. Prümper, U. Hergenhahn, M. Oura, M. Kitajima, T. Tanaka, H. Tanaka, S. Fritzsche, N. M. Kabachnik, and K. Ueda, Phys. Rev. A **70**, 040702 (2004), and reference therein.

[46] A. D. Fanis, G. Prümper, U. Hergenhahn, E. Kukk, T. Tanaka, M. Kitajima, H. Tanaka, S. Fritzsche, N. M. Kabachnik, and K. Ueda, J. Phys. B **38**, 2229 (2005), and references therein.

[47] B. Langer, A. Farhat, B. Nessar, N. Berrah, O. Hemmers, and J. D. Bozek, in *Proceedings, Atomic Physics with hard X-ray from High Brilliance Synchrotron Sources*, 1996 (unpublished), pp. 20–21.

[48] N. Berrah, B. Langer, A. A. Wills, E. Kukk, J. D. Bozek, A. Farhat, and T. W. Gorczyca, J. Electron Spectrosc. Relat. Phenom. **101**, 1 (1999).

[49] A. A. Wills, E. Sokell, T. W. Gorczyca, X. Feng, M. Wiedenhoeft, S. E. Canton, and N. Berrah, J. Phys. B **35**, L367 (2002).

[50] J. Jauhiainen, A. Ausmees, A. Kivimäki, S. J. Osborne, A. N. de Brito, S. Aksela, S. Svensson, and H. Aksela, J. Electron Spectrosc. Relat. Phenom. **69**, 181 (1994).

[51] L. O. Werme, T. Bergmark, and K. Siegbahn, Phys. Scr. **8**, 149 (1973).

[52] G. C. King, M. Tronc, F. H. Read, and R. C. Bradford, J. Phys. B **10**, 2479 (1977).

[53] Y. Hahn, Phys. Rev. A **13**, 1326 (1976).

[54] O. Nayandin, T. W. Gorczyca, A. A. Wills, B. Langer, J. D. Bozek, and N. Berrah, Phys. Rev. A **64**, 022505 (2001).

[55] H. Aksela, M. Kivilompolo, E. Nõmmiste, and S. Aksela, Phys. Rev. Lett. **79**, 4970 (1997).

[56] G. B. Armen and F. P. Larkins, J. Phys. B **24**, 741 (1991).

[57] G. B. Armen and F. P. Larkins, J. Phys. B **25**, 931 (1992).

[58] S. Svensson, B. Eriksson, N. Mårtensson, G. Wendin, and U. Gelius, J. Electron Spectrosc. Relat. Phenom. **47**, 327 (1988).

[59] M. O. Krause and F. H. Oliver, J. Phys. Chem. Ref. Data **8**, 329 (1979).